IOP PUBLISHING MEASUREMENT SCIENCE AND TECHNOLOGY

Meas. Sci. Technol. 18 (2007) 1661–1666 doi:10.1088/0957-0233/18/5/059

Practical spatial resolution limits of high-resolution fibre Bragg grating sensors using layer peeling*

R Joseph Espejo and Shellee D Dyer

National Institute of Standards and Technology, 325 Broadway, Boulder, CO 80305, USA

E-mail: sdyer@boulder.nist.gov

Received 12 January 2007, in final form 2 March 2007
Published 13 April 2007
Online at stacks.iop.org/MST/18/1661

Abstract
Inverse scattering methods such as layer peeling have been shown to reconstruct the longitudinal refractive index of fibre Bragg gratings with very high spatial resolution. These high spatial resolution measurements can be used to detect strain fields and thermal variations through the strain-optic and thermo-optic effects. However, physical constraints do not allow the refractive index to change on scales as short as these methods are capable of resolving. We demonstrate that this imposes a practical limitation of resolution on sensing applications. We use finite element modelling and compare this with experimental results. Longitudinal and transverse strains, as well as high resolution temperature sensing are considered. We show that the practical resolution limits are 40 μm for transverse stress sensing, 100 μm for longitudinal strain and 800 μm for thermal sensing.

Keywords: fibre Bragg gratings, fibre optic sensors, layer peeling, optical frequency-domain interferometry, temperature sensors, transverse strain sensors

Introduction

Fibre Bragg gratings (FBGs) have been shown to be an effective means of passively sensing environmental changes in strain and/or temperature. These environmental fluctuations affect the refractive index and grating pitch of the FBG. If the spatial extent of the applied strain or temperature field is large compared with the length of the grating, the field can be detected by monitoring the reflected wavelength. However, the spatial resolution limit is determined by the length of the FBG, which is often several millimetres at the shortest. Moreover, if the applied strain or temperature is nonuniform across the FBG, it can create ambiguities in the measured spectra, which can result in inaccurate measurements. This in effect limits the application of this type of sensors to areas of slowly-varying strain or temperature fields.

With the recent application of inverse scattering methods, such as the Born approximation method [1], a layer-peeling algorithm (LPA) [2] or a genetic algorithm [3], the refractive index changes due to environmental strain and temperature influences are detectable on scales smaller than the FBG length. This has been applied to measuring nonuniform strain fields as well as highly localized strains by direct measurement of the stress-optic or thermal-optic induced changes in the refractive index [3–12]. These methods have been shown to provide spatial resolutions near 10 μm, limited by the source bandwidth. However, the practical sensing limit can be much larger. This is limited by the elasticity and/or thermal conductivity of the fibre and host materials.

To investigate the limitations of high resolution sensing with FBGs we compare finite element (FE) models with experimental results. The FE models are used to investigate spatial extent of index perturbations due to localized strain and temperature impulses. The results are then compared with experimental results for validation. In particular, we examined the FBGs response to a highly localized applied stimulus and the half-width at half-maximum (HWHM) decay length of the resulting edge effects to determine how the sensor will perform in a spatially nonuniform strain field. The HWHM thus gives an estimation of the maximum practical resolution of the

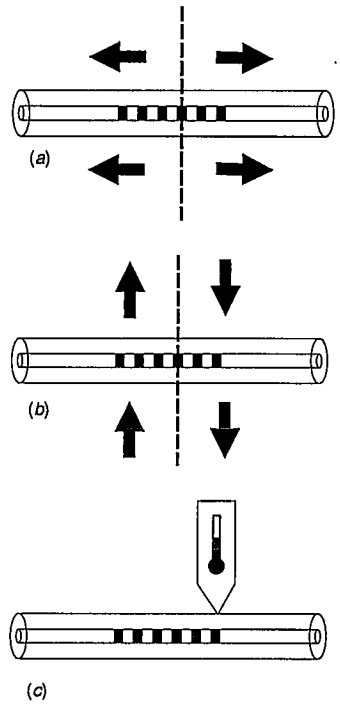

Figure 1. High resolution sensing scenarios: (*a*) localized longitudinal/axial strain from a crack or strain gradient; (*b*) localized transverse strain of shear; (*c*) localized temperature change or gradient.

FBG sensor. We examined three distinct cases: longitudinal strain, transverse strain and temperature sensing, as shown in figure 1.

The optical fibre used for the Bragg grating measurements is a low-doped germanosilicate single-mode fibre that is commonly used in telecom and sensing applications. For the physical parameters of the fibre we use $n_0 = 1.47$ as the refractive index in the unstressed fibre core, $\upsilon = 0.17$ for the Poisson ratio and $E = 7.3 \times 10^{10}$ Pa for Young's modulus [13], which are the properties of silica glass. For the purposes of the FE modelling, we assume that the small concentration of germanium will not significantly affect the spatial distribution of strain and temperature in the fibre, and we treat the entire fibre as a uniform cylinder of pure fused silica.

The measurement system, which is based on optical frequency-domain reflectometry (OFDR), is shown in figure 2. This measurement was previously discussed in [11]. The measurement interferometer is configured as a Fabry–Perot interferometer, with the sensing FBG forming one end of the cavity and an air/glass interface of a butt-coupling inside a capillary forming the other end. The distance between the butt-couple joint and the FBG is $d = 18$ cm, which forms a cavity with a free spectral range of 4.5 pm. For our sensing element we used a 1.5 cm long FBG with 11 dB peak reflectivity.

The laser's tuning nonlinearity is corrected using an unbalanced Mach–Zehnder reference interferometer. The reference signal is differentially detected and used to trigger the A/D sampling of the measurement interferometer at every zero crossing. The path imbalance used in the reference interferometer gives a sample spacing of about 0.5 pm, which over-samples the measurement Fabry–Perot interferometer signal at a rate of ten times per fringe. This signal is then digitized with a 16 bit A/D card.

The impulse response of the FBG is calculated from the inverse FFT. We window the impulse response at a delay equal to the time delay in the sensor cavity. The windowed impulse response is then Fourier transformed to produce the FBG's complex reflection spectrum. The FBG's longitudinal refractive index as a function of position is then found from the inverse scattering algorithm layer peeling, as in [2]. The spatial resolution of the calculated FBG index profile is inversely proportional to the bandwidth of the source, given by [2]

$$d_{\min} = \frac{1}{2n_0}\left(\frac{1}{\lambda_1} - \frac{1}{\lambda_2}\right)^{-1}, \qquad (1)$$

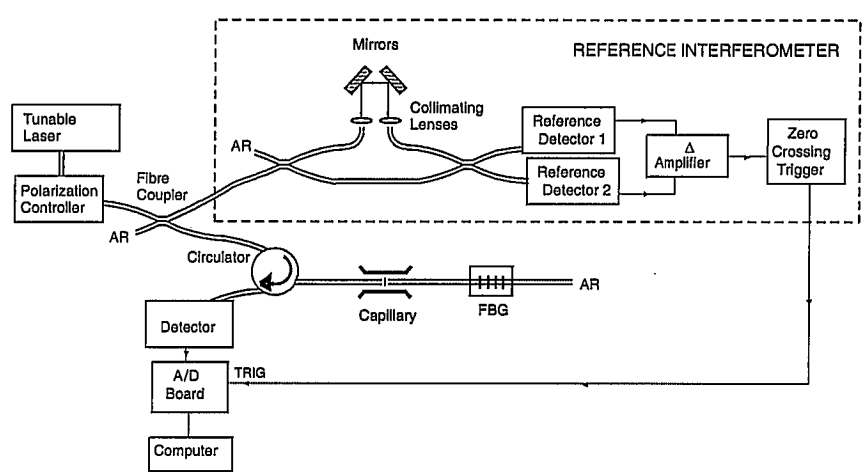

Figure 2. OFDR measurement system. Measurement interferometer is a Fabry–Perot configuration. An unbalanced Mach–Zehnder reference interferometer tracks the wavelength of the laser as it sweeps, triggering the A/D sampling in order to compensate for nonlinear tuning. The polarization controller sets the tunable laser light to the desired polarization launch state. AR: antireflection.

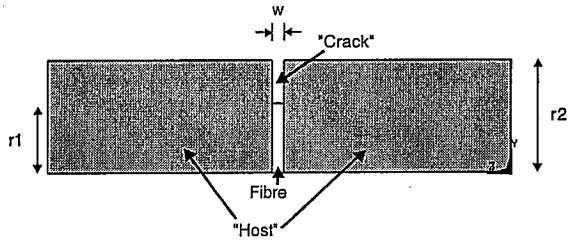

Figure 3. The quarter-symmetry geometry of the finite element model for transverse strain simulations. Longitudinal cross section is shown. A quarter-symmetry model was employed to minimize computation time. Cylinder radii: $r_1 = 125\ \mu m/2$ (fibre), $r_2 = 200\ \mu m/2$ (host), 'crack' width: $w = 10\ \mu m$.

where λ_1 and λ_2 are the extremes of the laser's tuning range. Given the laser's tuning range of 1511 nm to 1580 nm, $d_{min} = 11.8\ \mu m$ in air for our system.

Longitudinal strain

Longitudinal strains have two effects on the FBG's reflected wavelength: a physical change which causes a lengthening or contraction of the grating's pitch, and a photo-elastic change in the material's refractive index. The net effect on the reflected wavelength is given by [5]

$$\lambda(z) = \lambda_B((1 - p_e)\varepsilon_z(z) + 1), \qquad (2)$$

where $\lambda(z)$ is the position-dependent measured wavelength, λ_B is the unperturbed Bragg wavelength, $p_e = 0.215$ is the effective photo-elastic constant [5] and $\varepsilon_z(z)$ is the position-dependent longitudinal strain. High-resolution longitudinal strain measurements have been covered in detail by [4–7], and the resolution limits have recently been discussed in [7] to be less than 1 mm. Therefore we include no measurements of longitudinal strain; however, the FE models of longitudinal strain are included for completeness.

The FBG and surrounding host were modelled as a uniform cylinder of fused silica that was 200 μm in diameter, with a small waist section in the middle that was 10 μm wide and had the same diameter as bare fibre (125 μm), as shown in figure 3. Host diameters larger than 200 μm were tried, but with little effect on the results. Therefore, to optimize the computation, this smaller size was used. This geometry focuses the applied longitudinal pressure on the waist section. This would be a situation similar to a crack propagating through the host material perpendicular to the FBG. The size of the 'crack' was chosen to be the same as the resolution limit of the measurement system. This choice of dimension is somewhat arbitrary and does not significantly affect the results since we are mainly interested in how the fibre reacts at the edges of the localized applied strain. Additionally, the geometry of the FE simulation was chosen to mimic a real world situation that can be experimentally replicated. A small axial 'stretching' force of 10^{-5} N was applied to the end of the cylinder in the simulation while the other end was rigidly held. The small force was chosen to limit physical deformations.

The results of the FE simulations in figure 4 show a very broad distribution of the strain, extending well beyond the edges of the 'crack'. The HWHM is approximately 100 μm. These results are in agreement with the behaviour seen in [4–7].

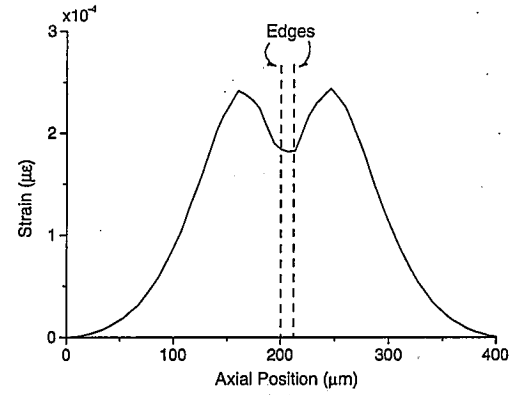

Figure 4. FE simulated longitudinal strain in the core of the geometry in figure 3. The locations of the edges of the crack are shown, labelled 'edges'.

Transverse strain

Transverse strains are a result of a pressure or shear force that is perpendicular to the FBG. When a transverse force is applied in the y-direction, the induced stress in the fibre causes an anisotropic change in the effective refractive index, n_{eff}, given by [14] as

$$\delta n_x = C_1\sigma_x + C_2\sigma_y \qquad \delta n_y = C_2\sigma_x + C_1\sigma_y, \qquad (3)$$

where δn_x and δn_y are the indices in the x- and y-directions. The constants $C_1 = -1.297 \times 10^{-6}$ mm^2 N^{-1} and $C_2 = -4.835 \times 10^{-6}$ mm^2 N^{-1} are defined as the stress-optic coefficients [14, 15]. The refractive indices in the x- and y-directions are then given by $n_x = n_o + \delta n_x$ and $n_y = n_o + \delta n_y$, with birefringence

$$\Delta n = \delta n_y - \delta n_x. \qquad (4)$$

We define the transverse stress difference

$$\sigma_x - \sigma_y = -\frac{\Delta n}{C_1 - C_2}, \qquad (5)$$

which is derived from equations (3) and (4).

To simulate a localized transverse strain, a uniform cylinder with the properties of fused silica representing the FBG was placed under a localized compressive load by a metallic block in a FE model. A quarter-symmetry model was used to minimize computation time. The geometry is shown in figure 5. A simulated uniform force is applied to the top of the metal block while the bottommost edge of the fibre is rigidly held. Only translations in the y-direction (vertical) were allowed; there were no rigid body rotations. The metallic block was thus allowed to slide downwards in the y-direction, come in contact with the fibre and apply a pressure on the contact surface. The FE model used a variable element size; the average element size was 0.1 μm.

The transverse stress values were computed along the axis of the cylinder, simulating the stress in the core of the FBG sensor. The FE stress was calculated for a 10 μm wide block. Again, the size of the simulated applied perturbation was

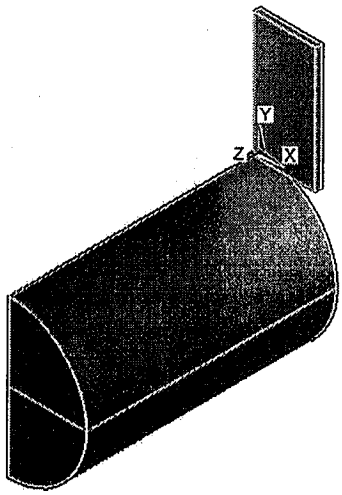

Figure 5. The geometry of the finite element model used for transverse strain simulations. A narrow (10 μm wide) metal block locally compresses a solid cylinder of fused silica. Again, a quarter-symmetry model is employed to minimize computation time.

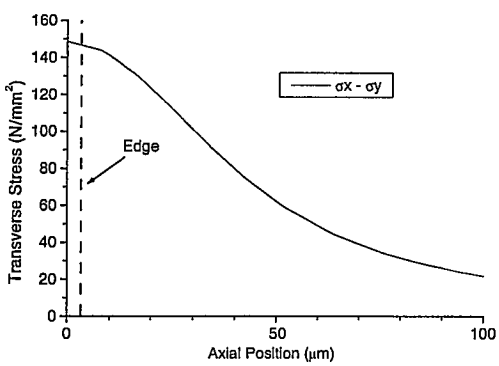

Figure 6. Results for FE simulated transverse stress ($\sigma_x - \sigma_y$) in the fibre from a 0.2 N load applied by a 10 μm wide block. 'Edge' marks the location of the edge of the stress-applying block in the simulation.

arbitrarily chosen to be the same as the fundamental resolution limit of the layer peeling algorithm, since only the effects at the edges of the perturbation were of interest. The results are shown in figure 6. The induced transverse stress in the FBG falls off gradually with a HWHM of 40 μm.

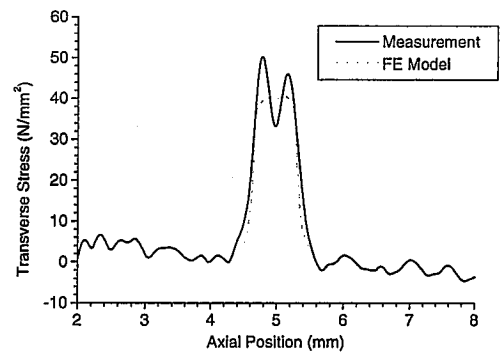

Figure 8. OFDR measured and calculated birefringence in the core of the FBG near the location of the localized strain created by the metal strip for a 2 N load.

Transverse loads are applied to the FBG with the fixture shown in figure 7, as previously described in [9, 11]. With this fixture a known compressive force of $mg/2$ can be applied to the FBG in a controlled manner by placing weights on the top of the fixture; m is the applied mass, and g is the gravitational constant. The test FBG and a support fibre are sandwiched between two thick polished glass plates. The support fibre ensures that the plates are parallel so that the compressive force is always perpendicular to the plates.

A 660 μm wide aluminium strip was placed under the FBG in the loading fixture to produce a localized transverse stress. The FBG was measured with the OFDR system. The birefringence, Δn, was then found with the LPA and a four polarization state method, as described in [9, 11]; the results are plotted in figure 8. Each measurement is the average of five sequential scans of the tunable laser. As predicted by the FE, the edges where the block makes contact with the fibre are not sharply resolved. Rather, the stress appears to drop off with a HWHM of approximately 30–50 μm, which correlates well with the FE results. Further, the cause of the peaks at the edges is most likely improper coupling between the aluminium strip and the FBG. It appears as though the fibre is bending around

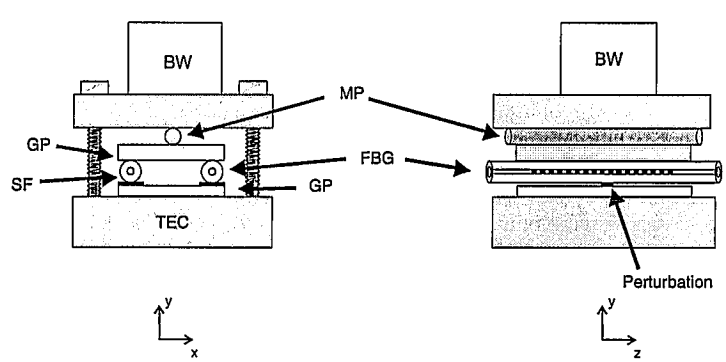

Figure 7. Schematic of the transverse loading fixture. SF: support fibre, GP: glass plate, MP: metal pin, BW: brass weight, TEC: thermoelectric cooler. Perturbation: 660 × 5000 × 50 μm^3 metal strip. Left: axial view. Right: side view.

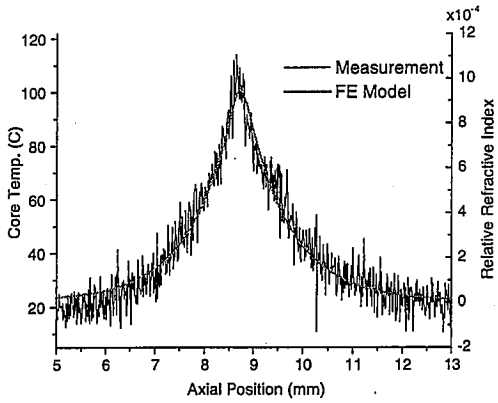

Figure 9. FE model and measurement for 80 °C (above ambient temperature) applied point-source temperature load.

the strip, causing a higher stress at the edges and lower in the centre. This non-uniform loading could explain the apparent noise in the measured peak birefringence in figure 7.

Temperature sensing

External environmental thermal loads have the overall effect of an increase in refractive index with increasing temperature [16]. The response to temperature has been shown to be approximately linear over a broad temperature range of −200 °C to 400 °C, making SiO_2 ideal for temperature sensing applications [16, 17]. Within the 1500–1600 nm wavelength range, the thermo-optic coefficient, dn/dT, is 1.19×10^{-5} [13].

The FE simulation was used to predict the temperature distribution from a point source of applied heat in order to then predict how the refractive index should change with position inside the FBG. The FBG was modelled as a uniform cylinder of fused silica, 125 μm in diameter. Allowances were made for convective cooling of its surface in air at 22 °C, the average room temperature at which the experiment was performed. For the properties of fused silica, the FE model used thermal conductivity = 1.38 W m^{-1} K^{-1}, specific heat = 703 J kg^{-1} K^{-1} and density = 2.203×10^3 kg m^{-3} [18]. The calculated equilibrium temperature values in the core of the cylinder are shown in figure 9. The HWHM is 965 μm for $\Delta T = 80$ °C, where ΔT is the change in temperature from ambient. For a smaller temperature change (not shown) of $\Delta T = 20$ °C, the HWHM is 820 μm.

For the experimental confirmation of this prediction, a localized thermal load was applied to the FBG by a heated knife-edge. The blade of the knife-edge was perpendicular to the fibre and was meant to approximate a point heat source. The temperature of the hot knife-edge was actively monitored and controlled to be 80 °C with a thermocouple near the tip and a commercial temperature controller.

The FBG was mounted suspended in air to isolate it from heat conducting surfaces that would cause unexpected results. The FBG was mounted with one end fixed and the other end attached to a movable stage as shown in figure 10. Constant tension was applied to the FBG by hanging a 20 g weight from

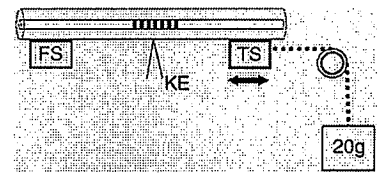

Figure 10. FBG mounting arrangement. Fibre is placed under light tension by a hanging weight as the hot knife-edge is applied. FS: fixed stage, TS: translating stage, KE: knife-edge.

a string attached to the movable stage. This ensured that the same tension was on the fibre even if the knife-edge caused the fibre to deflect.

The knife-edge was moved into position with a micrometre while being monitored with a microscope. We were careful to apply the knife-edge to the FBG with the same pressure for successive measurements so as to limit any anomalous results caused by mechanical strain. We wanted to achieve good physical contact between the knife-edge and the FBG without inducing any significant mechanical strain. This was accomplished by deflecting the FBG minimally and by the same amount, one fibre diameter. The measurement shown in figure 9 is the average of six sequential scans of the tunable laser. We believe that the high frequency noise is the result of strain from mechanical vibration due to the fibre being suspended in air. This vibrational strain can cause random variations in the refractive index at a rate that is faster than the measurement time, which adds to the error signal in the OFDR measurement. This noise is not seen in the mechanical strain measurements as the FBG is isolated and thermally stabilized in the loading fixture. The standard deviation of this noise in the measured refractive index is approximately 5×10^{-5}. A very good agreement is seen between the FE predictions and our measurements. The measured HWHM for $\Delta T = 80$ °C and for $\Delta T = 20$ °C are 980 μm and 860 μm, respectively.

Conclusions

We have shown that the actual physical limits to the spatial resolution of FBG sensors are larger than the resolution limits achievable by the inverse scattering algorithms. For transverse stress the limit is around 40 μm, assuming perfect coupling of the sensor to the host. For longitudinal strain, the limit is 100 μm; for temperature the limit is 800 μm.

These practical limitations should be taken into account when designing measurement systems. Deliberately band limiting the interferometric measurement so as to reduce the unnecessarily high resolution will have the positive effect of shortening the computation time of the FFT and LPA by reducing the number of unnecessary data points. This can easily be accomplished with OFDR systems by using equation (1) to determine the needed bandwidth, and then tuning the laser only through this wavelength range.

References

[1] Ohn M M, Huang S Y, Measures R M and Chwang J 1997 Arbitrary strain profile measurement within fibre gratings using interferometric Fourier transform technique *Electron. Lett.* **33** 1242–3

[2] Skaar J, Wang L and Erdogan T 2001 On the synthesis of fiber Bragg gratings by layer peeling *IEEE J. Quantum Electron* **37** 165–73

[3] Udd E 2006 Fiber grating sensors for structural health monitoring of aerospace structures *Proc. SPIE* **6167** 61670C-1

[4] Chapeleau X 2004 Accurate index profile measurements for fiber Bragg gratings and sensor applications *Symp. on Optical Fiber Measurements (NIST Spec. Publ.* vol 1024*)* pp 191–4

[5] Giaccari P, Dunkel G R, Humbert L, Botsis J, Limberger H G and Salathe R P 2005 On a direct determination of non-uniform internal strain fields using fibre Bragg gratings *Smart Mater. Struct.* **14** 127–36

[6] Eum S H, Kageyama K, Murayama H, Ohsawa I, Uzawa K and Kanai M 2006 Application of fiber Bragg grating distributed sensors to process and health monitoring of composite structures *18th Int. Optical Fiber Sensors Conf. Technical Digest (Washington, DC: Optical Society of America)* ThD4

[7] Murayama H, Igawa H, Kageyama K, Ohta K, Ohsawa I, Uzuwa K, Kanai M, Kasai T and Yamaguchi I 2006 Distributed strain measurement with high spatial resolution using fiber Bragg gratings and optical frequency domain reflectometry *18th Int. Optical Fiber Sensors Conf. Technical Digest (Washington, DC: Optical Society of America)* ThE40

[8] Chapeleau X, Leduc D, Lupi C, López-Gejo F, Douay M, Le Ny R and Boisrobert C 2006 Local characterization of fiber-Bragg gratings through combined use of low-coherence interferometry and a layer-peeling algorithm *Appl. Opt.* **45** 728–35

[9] Espejo R J and Dyer S D 2006 High spatial resolution measurements of transverse stress in a fiber Bragg grating using four-state analysis and layer-peeling *Proc. SPIE* **6167** 616707-1

[10] Udd E 2006 Fiber grating sensors for structural health monitoring of aerospace structures *Proc. SPIE* **6167** 61670C-1

[11] Espejo R J and Dyer S D 2006 Transverse stress measured by four-polarization-state frequency domain interferometry at high spatial resolution *18th Int. Optical Fiber Sensors Conf. Technical Digest (Washington, DC: Optical Society of America)* ThE43

[12] Coric D, Limberger H G and Salathe R P 2006 Distributed measurements of fiber birefringence and diametric load using optical low-coherence reflectometry and fiber gratings *Opt. Express* **14** 11804–13

[13] Driscoll W 1978 *Handbook of Optics* (New York: McGraw-Hill) p 174

[14] Lawrence C M, Nelson D V, Udd E and Bennett T 1999 A fiber optic sensor for transverse strain measurement *Exp. Mech.* **39** 202–9

[15] Wagreich R B, Altia E A, Singh H and Sirkis J S 1996 Effects of diametric load on fibre Bragg gratings in low birefringence fibre *Electron. Lett.* **32** 1223–4

[16] Simmons J 2000 *Optical Materials* (San Diego, CA: Academic) pp 108–10

[17] Gupta S, Mizunami T, Yamao T and Shimomura T 1996 Fiber Bragg grating cryogenic temperature sensors *Appl. Opt.* **35** 5202–5

[18] Morey G W 1954 *Properties of Glass* (New York: Reinhold) chapter 8